Information Sciences 504 (2019) 334–353

Contents lists available at ScienceDirect

Information Sciences

journal homepage: www.elsevier.com/locate/ins

Bilateral filter based total variation regularization for sparse hyperspectral image unmixing☆

Xiao Li, Jie Huang*, Liang-Jian Deng, Ting-Zhu Huang

School of Mathematical Sciences, University of Electronic Science and Technology of China, Chengdu, Sichuan, 611731, PR China

ARTICLE INFO

Article history:
Received 19 April 2019
Revised 15 July 2019
Accepted 16 July 2019
Available online 16 July 2019

Keywords:
Hyperspectral images
Spectral unmixing
Bilateral filter
Total variation
The alternating direction method of multipliers (ADMM)

ABSTRACT

Spectral unmixing of hyperspectral images aims to find the proportion of constituent materials in mixed pixels. The total variation (TV) regularization is widely included in classical sparse regression formulations to exploit the spatial information in hyperspectral data. It promotes piecewise constant transitions in the fractional abundance of the same endmember among neighboring pixels. The TV regularization term, however, usually brings some staircase effects. To alleviate this drawback, we propose a bilateral filter based TV regularization for hyperspectral image unmixing. Then we present an unmixing model that combines a data-fidelity term, a sparsity regularization term, and the new regularization term. To solve the proposed model, we design an algorithm called sparse unmixing via variable splitting augmented Lagrangian and bilateral filter based TV (SUnSAL-BF-TV), under the alternating direction method of multipliers (ADMM) framework. Our experimental results show that our algorithm is effective to unmix both simulated and real hyperspectral data sets.

1. Introduction

Spectral unmixing aims to find the proportion of constituent materials in a mixed pixel in hyperspectral images (HSIs) [1]. The linear mixture model (LMM) is widely adopted for the spectral unmixing problem due to its flexibility and tractability. It assumes that each mixed pixel can be expressed as a linear combination of *endmembers* with corresponding *abundances* [2–4]. Due to physical background, these abundances often satisfy *the abundance nonnegativity constraint* (ANC) and *the abundance sum-to-one constraint* (ASC) [5].

Sparse unmixing algorithms characterize the mixed pixels by finding the optimal subset of signatures from a (potentially very large) spectral library [6–9]. The classic sparse unmixing assumes that each mixed pixel is composed of few endmembers, and thus the resulting abundance vector is sparse. Commonly, an ℓ_1 regularization is employed to promote the sparsity character [6,7,10–13]. Other sparsity-based regularizers are adopted to further encourage the sparseness and improve the unmixing performance [8,14–16]. Also, iteratively reweighted strategies have been incorporated into sparse unmixing to obtain better performance [9,17–19].

Exploiting spatial information of hyperspectral data becomes another efficient way to improve the unmixing performance [16,19–24]. Specifically, the total variation (TV) spatial regularization is included in spectral unmixing to promote that neigh-

☆ This research is supported in part by NSFC under Grants 61772003, 61876203, and 61702083 and in part by Science Strength Promotion Programme of UESTC.

* Corresponding author.
E-mail address: huangjie_uestc@uestc.edu.cn (J. Huang).

https://doi.org/10.1016/j.ins.2019.07.063
0020-0255/

boring pixels have both similar mixing materials and similar fractional abundances [14,21,22,25–29]. This assumption is rather strict and commonly causes some staircase effects. The collaborative sparse regression for the hyperspectral unmixing problem enforces that all the pixels in some scene share the same support set of materials but do not necessarily have similar abundance for each material [15,19,25,30]. Thus, the collaborative sparsity is less strict than the TV regularization. Recently, the low-rank representation has become a powerful tool for studying spatial information of HSIs [19,23,24,31–35]. Consider that the homogeneous regions of HSIs exist a high degree of correlation among the spectral signatures of neighboring pixels. Then the correlation is reflected as linear dependence of their corresponding abundance vectors and leads to a low-rank abundance matrix [19,23,24]. In addition, the nonlocal means method, as a spatial regularizer, is used to exploit the nonlocal spatial information in the abundance map [36]. More recently, the centralized collaborative sparse unmixing has coupled collaborative sparse unmixing and abundance estimation error reduction together [37]. And a robust sparse unmixing adopts an $\ell_{2,1}$ norm loss function, which is robust for noises and outliers [38]. That said, incorporating spatial information improves the abundance estimation accuracy.

In this paper, we propose to include the bilateral filter into the TV regularization framework for the hyperspectral image unmixing problem. Recall that the TV regularization is employed on each abundance map and so promotes piecewise smooth transitions in these abundance maps, which usually brings some staircase effects. To address this drawback, we propose a bilateral filter based TV regularizer for hyperspectral image unmixing. That is, we first apply the bilateral filter to each abundance map such that the bilateral filtered abundance maps are more smooth while preserving sharp edges. It follows that the piecewise constant transitions character in the bilateral filtered abundance maps is more prominent than that in the original abundance maps (we will show a simple example in Section 2.2). Then we impose the TV regularizer on these bilateral filtered abundance maps. That said, we want to improve the unmixing performance by imposing the TV regularizer on bilateral filtered abundance maps, rather than directly on the abundance maps themselves, commonly as in [14,21,22] and so on. Following this line, we present a model that combines the bilateral filter based TV term, the sparsity regularization term, and the data-fidelity term. And to solve the proposed model, we design an algorithm called sparse unmixing via variable splitting augmented Lagrangian and bilateral filter based TV (SUnSAL-BF-TV), under *the alternating direction method of multipliers* (ADMM) framework. Our experimental results will show that the proposed algorithm provides better unmixing performance for both simulated and real hyperspectral data sets, in comparison with several popular hyperspectral unmixing algorithms.

The main contributions of this paper could be summarized as follows.

(1) We propose a bilateral filter based TV regularizer to relax the piecewise constant transitions assumption of the TV regularization for the hyperspectral unmixing problem. The new regularizer alleviates the staircase effects caused by the TV term.
(2) We propose a hyperspectral unmixing model that combines a data-fidelity term, an ℓ_1-norm-based sparse regularization term, and a bilateral filter based TV regularization term. Also, a reweighted matrix is used to further promote the sparseness of the abundance.
(3) To solve the proposed model, we design an algorithm called SUnSAL-BF-TV under the ADMM framework. Numerical experiments show the effectiveness of the proposed algorithm on both simulated and real hyperspectral data.

The remainder of this paper is organized as follows. Section 2 describes the problem formulation for the hyperspectral image unmixing and briefly reviews the bilateral filter. Section 3 presents the proposed model and corresponding sparse unmixing algorithm. The effectiveness of the proposed algorithm is demonstrated on both simulated hyperspectral data sets in Section 4 and real data in Section 5. Finally, Section 6 concludes with some remarks.

2. Background

2.1. Problem formulation

Let $\mathbf{Y} \in \mathbb{R}^{L\times n}$ be the hyperspectral image with L bands and n pixels. Let $\mathbf{A} \in \mathbb{R}^{L\times m}$ be the spectral library with the jth column being the spectral signature of the jth endmember, for $j = 1, \ldots, m$, and $\mathbf{X} \in \mathbb{R}^{m\times n}$ is the fractional abundance matrix. Then the LMM assumes

$$\mathbf{Y} = \mathbf{AX} + \mathbf{N},$$

where $\mathbf{N} \in \mathbb{R}^{L\times n}$ is an independent and identically distributed (i.i.d.) zero-mean Gaussian noise matrix. Commonly, the ANC, i.e., $\mathbf{X} \geq \mathbf{0}$, and the ASC, i.e., $\mathbf{1}^T\mathbf{X} = \mathbf{1}$, are imposed on $\mathbf{X}$ based on physically meaning. Here, the inequality $\mathbf{X} \geq \mathbf{0}$ is considered entrywise nonnegative and $\mathbf{1}$ is a column vector of 1s. Similarly, as in [15,21,24], we relax the ASC to focus on exploiting the sparseness of the fractional abundances.

Sparse unmixing assumes that each mixed pixel in an HSI is a linear combination of a few of endmembers, with a known large spectral library $\mathbf{A}$ [6]. Then the sparse unmixing is to solve an optimization problem

$$\min_{\mathbf{X}} \quad \frac{1}{2}\|\mathbf{AX} - \mathbf{Y}\|_F^2 + \lambda\|\mathbf{X}\|_0, \quad \text{s.t.} \quad \mathbf{X} \geq \mathbf{0},$$

where $\|\cdot\|_F$ is the Frobenius norm, $\|\mathbf{X}\|_0$ is the ℓ_0 norm of $\mathbf{X}$, and $\lambda \geq 0$ is a regularization parameter. Due to the non-convex character of the ℓ_0 term, this problem is NP-hard and difficult to solve. One popular solution is to relax the ℓ_0 norm with

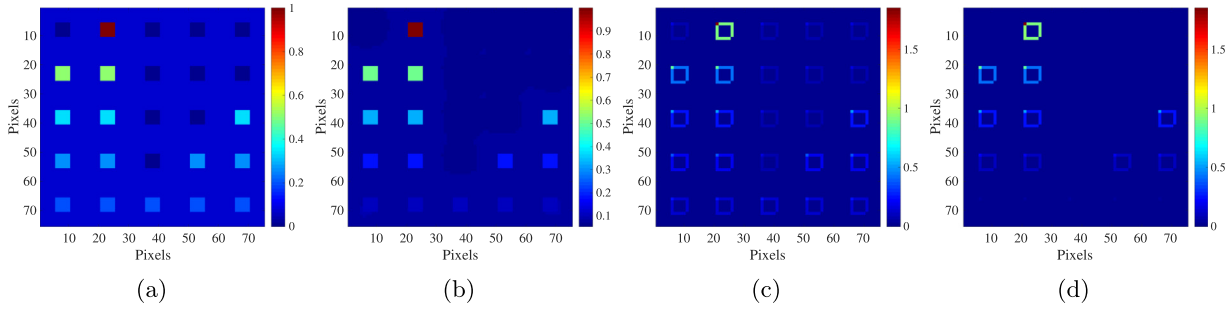

Fig. 1. The effectiveness of coupling the bilateral filtering with the difference operator. (a) True abundance map X. (b) $\mathbf{BF}(X)$. (c) $\mathbf{D}(X)$. (d) $\mathbf{D}(\mathbf{BF}(X))$. In this example, $\mathbf{D}(\mathbf{BF}(X))$ is more sparse than $\mathbf{D}(X)$. Thus, we hope to improve the unmixing performance by imposing TV term on $\mathbf{BF}(X)$ instead of on X.

the ℓ_1 norm. Then the following optimization problem is obtained in [6]:

$$\min_{\mathbf{X}} \quad \frac{1}{2}\|\mathbf{AX}-\mathbf{Y}\|_F^2 + \lambda\|\mathbf{X}\|_{1,1}, \quad \text{s.t.} \quad \mathbf{X} \geq \mathbf{0},$$

where $\|\mathbf{X}\|_{1,1} = \sum_{i=1}^{m}\sum_{j=1}^{n}|x_{i,j}|$ with x_{ij} being the (i, j)th entry of $\mathbf{X}$.

In order to improve the unmixing performance, a TV regularizer is introduced to promote spatial homogeneity among neighboring pixels [21]. The resulting optimization model is

$$\min_{\mathbf{X}} \frac{1}{2}\|\mathbf{AX}-\mathbf{Y}\|_F^2 + \lambda\|\mathbf{X}\|_{1,1} + \lambda_{TV}\mathbf{TV}(\mathbf{X}), \quad \text{s.t.} \quad \mathbf{X} \geq \mathbf{0},$$

where $\lambda \geq 0$ and $\lambda_{TV} \geq 0$ are regularization parameters,

$$\mathbf{TV}(\mathbf{X}) \equiv \|\mathbf{HX}\|_{1,1}, \tag{1}$$

and $\mathbf{H}$ is defined by

$$\mathbf{HX} \equiv \begin{bmatrix}\mathbf{H}_h\mathbf{X} \\ \mathbf{H}_v\mathbf{X}\end{bmatrix}.$$

Here, $\mathbf{H}_h$ ($\mathbf{H}_v$, respectively): $\mathbb{R}^{m\times n} \to \mathbb{R}^{m\times n}$ is a linear operator computing the horizontal (vertical, respectively) difference between the components of $\mathbf{X}$ corresponding to neighboring pixels. Especially, the boundary condition is assumed as being periodic; see also [39,40].

2.2. Bilateral filter

Before introducing a new regularizer based on the bilateral filter and TV, we first briefly review the bilateral filter. It is well-known that the bilateral filter can smooth images while preserving edges by means of non-linear combination of nearby values [41,42]. The bilateral filter, denoted by $\mathbf{BF}(\cdot)$, is defined by:

$$\mathbf{BF}(I)_p = \frac{1}{\mathrm{W}_p}\sum_{q\in\mathrm{S}} \mathrm{G}_{\sigma_s}(\|p-q\|)\mathrm{G}_{\sigma_r}(|I_p - I_q|)I_q. \tag{2}$$

Here I denotes the input image, I_p is the image value at pixel position p, S is the spatial domain, and $\Sigma_{q\in\mathrm{S}}$ denotes a sum over all image pixels indexed by q. $\mathrm{G}_\sigma(x)$ denotes the 2-D Gaussian kernel:

$$\mathrm{G}_\sigma(x) = \frac{1}{2\pi\sigma^2}\exp\left(-\frac{x^2}{2\sigma^2}\right),$$

where σ is a parameter defining the neighborhood size. Here σ_s and σ_r are *spatial* and *range* parameters for the spatial Gaussian weighting G_{σ_s} and the range Gaussian weighting G_{σ_r}, respectively. And $\|p-q\|$ is the Euclidean distance between pixel locations p and q. The normalization constant W_p in (2) ensures all pixel weights sum to one:

$$\mathrm{W}_p = \sum_{q\in\mathrm{S}} \mathrm{G}_{\sigma_s}(\|p-q\|)\mathrm{G}_{\sigma_r}(|I_p - I_q|).$$

Clearly, the bilateral filter is a combination of spatial and range filters.

We now give a simple example to visually show the effectiveness of the combination of bilateral filtering with TV. Note that the TV regularizer promotes sparsity in the gradient domain. Fig. 1(a) shows an original abundance map $X \in \mathbb{R}^{75\times 75}$, which has been widely used for the hyperspectral image unmixing problem (see [14,19,21,43]). Then, under periodic boundary conditions, we define a difference operator $\mathbf{D}$ as

$$(\mathbf{D}(X))_{i,j} = |x_{i+1,j} - x_{i,j}| + |x_{i,j+1} - x_{i,j}|,$$

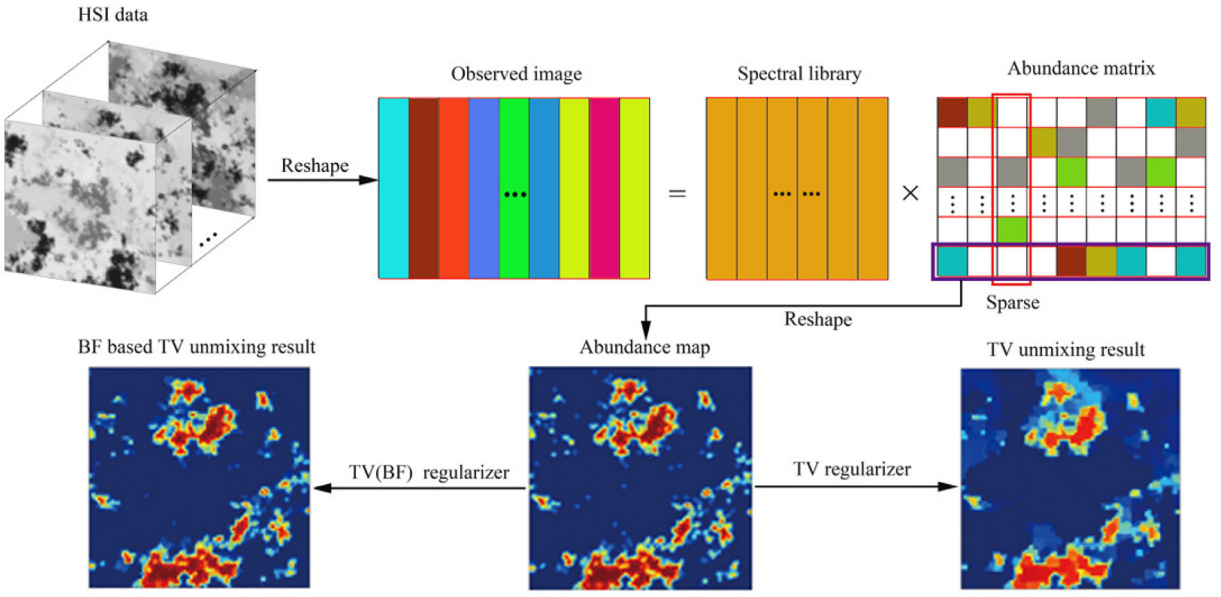

Fig. 2. Flowchart of the proposed unmixing algorithm.

where $x_{i,j}$ and $(\mathbf{D}(X))_{i,j}$ are the (i, j)th entries of X and $\mathbf{D}(X)$, respectively. It is clear from (1) and the definition of $\mathbf{D}$ that

$$\mathbf{TV}(X) = \|\mathbf{H}X\|_{1,1} = \|\mathbf{D}(X)\|_{1,1}.$$

Fig. 1(b) and (c) show the result of bilateral filtering $\mathbf{BF}$ and the result of $\mathbf{D}$ after applying to X, denoted as $\mathbf{BF}(X)$ and $\mathbf{D}(X)$, respectively. Finally, the result of the difference operator $\mathbf{D}$ on $\mathbf{BF}(X)$, i.e., $\mathbf{D}(\mathbf{BF}(X))$, is shown in Fig. 1(d).

From Fig. 1(b), we see that the bilateral filter smoothes the image while maintaining the sharp boundaries as expected. We can also see from Fig. 1(c) and (d) that $\mathbf{D}(\mathbf{BF}(X))$ is more sparse than $\mathbf{D}(X)$. It is therefore hoped to improve the unmixing performance by exploiting the sparsity of $\mathbf{D}(\mathbf{BF}(X))$. To this end, we propose to apply the TV term on $\mathbf{BF}(X)$ instead of on X in the next section.

3. Proposed model and algorithm

For hyperspectral image unmixing, we now propose a bilateral filter based TV regularizer to further exploit the sparsity in the gradient domain. In addition, we use a weighting ℓ_1 regularization by adopting a weighting matrix $\mathbf{W}$ to further enforce the sparsity of $\mathbf{X}$, as in [19,24,44]. Then we carry out the sparse unmixing by solving the following optimization problem:

$$\min_{\mathbf{X}} \ \frac{1}{2}\|\mathbf{AX} - \mathbf{Y}\|_F^2 + \lambda\|\mathbf{W} \odot \mathbf{X}\|_{1,1} + \lambda_{bf}\mathbf{TV}(\mathbf{BF}(\mathbf{X})) \quad \text{s.t.} \quad \mathbf{X} \geq \mathbf{0}, \tag{3}$$

where the denotation $\odot$ represents the elementwise multiplication (i.e., Hadamard product) of the nonnegative weighing matrix $\mathbf{W}$ and $\mathbf{X}$, and $\lambda \geq 0$ and $\lambda_{bf} \geq 0$ are regularization parameters. We note that the next weighting matrix is computed from the value of the current solution. In the literature, this reweighting strategy has been widely used to promote the sparsity for ℓ_1-norm-based regularized problems [24,27,44]. We will specify the value of $\mathbf{W}$ in the following proposed algorithm. Before that, we first give a flowchart of the proposed algorithm in Fig. 2. As presented, we integrate the sparseness prior and the spatial-contextual information for hyperspectral unmixing. Specifically, the bilateral filter is included in the classic TV regularization to remove the staircase effects.

We now solve the model in (3). It is clear that all terms in the objective function are coupled together concerning $\mathbf{X}$. Thus, it is hard to obtain $\mathbf{X}$ directly. To address this drawback, we design an algorithm under the ADMM framework to decompose the original problem into several smaller subproblems. For this purpose, we first rewrite (3) to be the following equivalent constrained problem:

$$\begin{aligned} &\min_{\mathbf{X},\mathbf{V}_i,i=1,\ldots,6} \frac{1}{2}\|\mathbf{V}_1 - \mathbf{Y}\|_F^2 + \lambda\|\mathbf{W} \odot \mathbf{V_2}\|_{1,1} + \lambda_{bf}\|\mathbf{V}_5\|_{1,1} + \iota_{R_+}(\mathbf{V}_6), \\ &\text{s.t.} \quad \mathbf{AX} = \mathbf{V}_1, \mathbf{X} = \mathbf{V}_2, \mathbf{X} = \mathbf{V}_3, \mathbf{BF}(\mathbf{V}_3) = \mathbf{V}_4, \mathbf{HV}_4 = \mathbf{V}_5, \mathbf{X} = \mathbf{V}_6, \end{aligned} \tag{4}$$

where ι_Ω is the indicator function of a set Ω, i.e., $\iota_\Omega(x) = 0$ if $x \in \Omega$ and $\iota_\Omega(x) = +\infty$ otherwise. We see a constraint in (4): $\mathbf{BF}(\mathbf{V}_3) = \mathbf{V}_4$, with the bilateral filter $\mathbf{BF}$. Notice that the $\mathbf{BF}$ is a non-linear operator and so we temporarily use the $\mathbf{KV}_3$ to

linearly replace the $\mathbf{BF}(\mathbf{V}_3)$ such that we can design an algorithm under the ADMM framework. We will specify the matrix $\mathbf{K}$ in the corresponding subproblems. Define

$$\mathbf{G}=\begin{bmatrix}\mathbf{A}\\ \mathbf{I}\\ \mathbf{I}\\ \mathbf{0}\\ \mathbf{0}\\ \mathbf{I}\end{bmatrix},\quad \mathbf{V}=\begin{bmatrix}\mathbf{V}_1\\ \mathbf{V}_2\\ \mathbf{V}_3\\ \mathbf{V}_4\\ \mathbf{V}_5\\ \mathbf{V}_6\end{bmatrix},\quad \mathbf{B}=\begin{bmatrix}-\mathbf{I} & \mathbf{0} & \mathbf{0} & \mathbf{0} & \mathbf{0} & \mathbf{0}\\ \mathbf{0} & -\mathbf{I} & \mathbf{0} & \mathbf{0} & \mathbf{0} & \mathbf{0}\\ \mathbf{0} & \mathbf{0} & -\mathbf{I} & \mathbf{0} & \mathbf{0} & \mathbf{0}\\ \mathbf{0} & \mathbf{0} & \mathbf{K} & -\mathbf{I} & \mathbf{0} & \mathbf{0}\\ \mathbf{0} & \mathbf{0} & \mathbf{0} & \mathbf{H} & -\mathbf{I} & \mathbf{0}\\ \mathbf{0} & \mathbf{0} & \mathbf{0} & \mathbf{0} & \mathbf{0} & -\mathbf{I}\end{bmatrix},$$

where $\mathbf{I}$ is the identity matrix. Let

$$g(\mathbf{V})=\frac{1}{2}\|\mathbf{V}_1-\mathbf{Y}\|_F^2+\lambda\|\mathbf{W}\odot\mathbf{V}_2\|_{1,1}+\lambda_{bf}\|\mathbf{V}_5\|_{1,1}+\iota_{R_+}(\mathbf{V}_6).$$

Then we obtain the optimization problem:

$$\min_{\mathbf{X},\mathbf{V}} g(\mathbf{V})\quad \text{s.t.}\quad \mathbf{GX}+\mathbf{BV}=\mathbf{0}. \tag{5}$$

Introducing Lagrange multipliers $\mathbf{D}=[\mathbf{D}_1^T,\mathbf{D}_2^T,\mathbf{D}_3^T,\mathbf{D}_4^T,\mathbf{D}_5^T,\mathbf{D}_6^T]^T$ and define

$$\mathcal{L}(\mathbf{X},\mathbf{V},\mathbf{D})=g(\mathbf{V})+\frac{\mu}{2}\|\mathbf{GX}+\mathbf{BV}-\mathbf{D}\|_F^2,$$

where $\mu>0$ is a penalty parameter. We minimize $\mathcal{L}(\mathbf{X},\mathbf{V},\mathbf{D})$ with respect to $\mathbf{X}$ and $\mathbf{V}$ and update $\mathbf{D}$ under the ADMM framework

$$\begin{cases}\mathbf{X}^{(k+1)}=\operatorname{argmin}_{\mathbf{X}}\mathcal{L}(\mathbf{X},\mathbf{V}^{(k)},\mathbf{D}^{(k)})\\ \mathbf{V}^{(k+1)}=\operatorname{argmin}_{\mathbf{V}}\mathcal{L}(\mathbf{X}^{(k+1)},\mathbf{V},\mathbf{D}^{(k)})\\ \mathbf{D}^{(k+1)}=\mathbf{D}^{(k)}-\mathbf{GX}^{(k+1)}-\mathbf{BV}^{(k+1)}\end{cases}, \tag{6}$$

until some stopping criterion is satisfied.

For (6), we first compute $\mathbf{X}$ by solving the optimization problem

$$\min_{\mathbf{X}}\left\|\mathbf{AX}-\mathbf{V}_1^{(k)}-\mathbf{D}_1^{(k)}\right\|_F^2+\left\|\mathbf{X}-\mathbf{V}_2^{(k)}-\mathbf{D}_2^{(k)}\right\|_F^2+\left\|\mathbf{X}-\mathbf{V}_3^{(k)}-\mathbf{D}_3^{(k)}\right\|_F^2+\left\|\mathbf{X}-\mathbf{V}_6^{(k)}-\mathbf{D}_6^{(k)}\right\|_F^2.$$

It is easy to obtain that

$$\mathbf{X}^{(k+1)}=(\mathbf{A}^T\mathbf{A}+3\mathbf{I})^{-1}(\mathbf{A}^T(\mathbf{V}_1^{(k)}+\mathbf{D}_1^{(k)})+\mathbf{V}_2^{(k)}+\mathbf{D}_2^{(k)}+\mathbf{V}_3^{(k)}+\mathbf{D}_3^{(k)}+\mathbf{V}_6^{(k)}+\mathbf{D}_6^{(k)}),$$

where $\mathbf{A}^T$ represents the transpose of $\mathbf{A}$.

For the $\mathbf{V}$ subproblem in (6), we decouple it to 6 subproblems with respect to $\mathbf{V}_i$, for $i=1,\ldots,6$. For $\mathbf{V}_1$, it is to solve the optimization problem

$$\min_{\mathbf{V}_1}\frac{1}{2}\|\mathbf{V}_1-\mathbf{Y}\|_F^2+\frac{\mu}{2}\left\|\mathbf{AX}^{(k+1)}-\mathbf{V}_1-\mathbf{D}_1^{(k)}\right\|_F^2.$$

It clearly follows that

$$\mathbf{V}_1^{(k+1)}=\frac{1}{1+\mu}\left(\mathbf{Y}+\mu(\mathbf{AX}^{(k+1)}-\mathbf{D}_1^{(k)})\right).$$

Then $\mathbf{V}_2^{(k+1)}$ is computed by solving the optimization problem

$$\min_{\mathbf{V}_2}\lambda\|\mathbf{W}\odot\mathbf{V}_2\|_{1,1}+\frac{\mu}{2}\left\|\mathbf{X}^{(k+1)}-\mathbf{V}_2-\mathbf{D}_2^{(k)}\right\|_F^2. \tag{7}$$

Here we adopt a *reweighting* strategy for the weighting matrix $\mathbf{W}$, similarly as in [17,19,24,44]. That is, the weights used for the next iteration are obtained from the value of the current solution. In this spirit, with obtained $\mathbf{X}^{(k+1)}$ and $\mathbf{D}_2^{(k)}$, define

$$\mathbf{W}_{i,j}^{(k)}=\frac{1}{\left|\left(\mathbf{X}^{(k+1)}-\mathbf{D}_2^{(k)}\right)_{i,j}\right|+\epsilon},$$

where $\epsilon=10^{-16}$ is a small positive value to avoid singularities. Consider the "weighted" ℓ_1 minimization problem:

$$\min_{\mathbf{V}_2}\lambda\left\|\mathbf{W}^{(k)}\odot\mathbf{V}_2\right\|_{1,1}+\frac{\mu}{2}\left\|\mathbf{X}^{(k+1)}-\mathbf{V}_2-\mathbf{D}_2^{(k)}\right\|_F^2. \tag{8}$$

Clearly, the solution of (8) is

$$\mathbf{V}_2^{(k+1)}=\operatorname{soft}(\mathbf{X}^{(k+1)}-\mathbf{D}_2^{(k)},\tfrac{\lambda}{\mu}\mathbf{W}^{(k)}).$$

Here soft$(\cdot,\cdot)$ is a non-linear soft-thresholding operator defined component-wise by

$$(\text{soft}(\mathbf{U},\alpha))_{i,j} = \text{sign}(\mathbf{U}_{i,j})\max\{|\mathbf{U}_{i,j}| - \alpha, 0\},$$

for $\forall\, \mathbf{U} \in \mathbb{R}^{m\times n}$ and $\alpha \geq 0$.

The subproblem concerning $\mathbf{V}_3$ is

$$\min_{\mathbf{V}_3} \left\|\mathbf{X}^{(k+1)} - \mathbf{V}_3 - \mathbf{D}_3^{(k)}\right\|_F^2 + \left\|\mathbf{K}\mathbf{V}_3 - \mathbf{V}_4^{(k)} - \mathbf{D}_4^{(k)}\right\|_F^2.$$

Here for computational convenience, we use the identity matrix $\mathbf{I}$ to replace the matrix $\mathbf{K}$ and obtain that

$$\min_{\mathbf{V}_3} \left\|\mathbf{X}^{(k+1)} - \mathbf{V}_3 - \mathbf{D}_3^{(k)}\right\|_F^2 + \left\|\mathbf{V}_3 - \mathbf{V}_4^{(k)} - \mathbf{D}_4^{(k)}\right\|_F^2.$$

Then it is easy to get that

$$\mathbf{V}_3^{(k+1)} = \frac{1}{2}(\mathbf{V}_4^{(k)} + \mathbf{D}_4^{(k)}) + \frac{1}{2}(\mathbf{X}^{(k+1)} - \mathbf{D}_3^{(k)}).$$

In order to compute $\mathbf{V}_4$, we solve the optimization problem

$$\min_{\mathbf{V}_4} \left\|\mathbf{K}\mathbf{V}_3^{(k+1)} - \mathbf{V}_4 - \mathbf{D}_4^{(k)}\right\|_F^2 + \left\|\mathbf{H}\mathbf{V}_4 - \mathbf{V}_5^{(k)} - \mathbf{D}_5^{(k)}\right\|_F^2.$$

Recall that we use the $\mathbf{K}\mathbf{V}_3$ to linearly replace the $\mathbf{BF}(\mathbf{V}_3)$ in (5). Without this replacement, we also obtain a least-squares problem

$$\min_{\mathbf{V}_4} \|\mathbf{BF}(\mathbf{V}_3^{(k+1)}) - \mathbf{V}_4 - \mathbf{D}_4^{(k)}\|_F^2 + \|\mathbf{H}\mathbf{V}_4 - \mathbf{V}_5^{(k)} - \mathbf{D}_5^{(k)}\|_F^2.$$

Then easily we have

$$\mathbf{V}_4^{(k+1)} = (\mathbf{I} + \mathbf{H}^T\mathbf{H})^{-1}\left(\mathbf{BF}(\mathbf{V}_3^{(k+1)}) - \mathbf{D}_4^{(k)} + \mathbf{H}^T(\mathbf{V}_5^{(k)} + \mathbf{D}_5^{(k)})\right).$$

For the $\mathbf{V}_5$ subproblem, we have

$$\min_{\mathbf{V}_5} \lambda_{bf}\|\mathbf{V}_5\|_{1,1} + \frac{\mu}{2}\left\|\mathbf{H}\mathbf{V}_4^{(k+1)} - \mathbf{V}_5 - \mathbf{D}_5^{(k)}\right\|_F^2.$$

It follows that

$$\mathbf{V}_5^{(k+1)} = \text{soft}(\mathbf{H}\mathbf{V}_4^{(k+1)} - \mathbf{D}_5^{(k)}, \frac{\lambda_{bf}}{\mu}).$$

Then for $\mathbf{V}_6$, it is to solve the optimization problem:

$$\min_{\mathbf{V}_6} \iota_{R_+}(\mathbf{V}_6) + \frac{\mu}{2}\left\|\mathbf{X}^{(k+1)} - \mathbf{V}_6 - \mathbf{D}_6^{(k)}\right\|_F^2.$$

Simple calculation shows that

$$\mathbf{V}_6^{(k+1)} = \max(\mathbf{X}^{(k+1)} - \mathbf{D}_6^{(k)}, \mathbf{0}).$$

Finally, we update all Lagrange multipliers

$$\begin{cases} \mathbf{D}_1^{(k+1)} = \mathbf{D}_1^{(k)} - \mathbf{A}\mathbf{X}^{(k+1)} + \mathbf{V}_1^{(k+1)} \\ \mathbf{D}_2^{(k+1)} = \mathbf{D}_2^{(k)} - \mathbf{X}^{(k+1)} + \mathbf{V}_2^{(k+1)} \\ \mathbf{D}_3^{(k+1)} = \mathbf{D}_3^{(k)} - \mathbf{X}^{(k+1)} + \mathbf{V}_3^{(k+1)} \\ \mathbf{D}_4^{(k+1)} = \mathbf{D}_4^{(k)} - \mathbf{BF}(\mathbf{V}_3^{(k+1)}) + \mathbf{V}_4^{(k+1)} \\ \mathbf{D}_5^{(k+1)} = \mathbf{D}_5^{(k)} - \mathbf{H}\mathbf{V}_4^{(k+1)} + \mathbf{V}_5^{(k+1)} \\ \mathbf{D}_6^{(k+1)} = \mathbf{D}_6^{(k)} - \mathbf{X}^{(k+1)} + \mathbf{V}_6^{(k+1)}. \end{cases}$$

To make it more clear, we summarize the proposed sparse hyperspectral image unmixing algorithm, denoted as SUnSAL-BF-TV, as follows (Algorithm 1).

We note that the SUnSAL-BF-TV algorithm is similar to SUnSAL-TV in [21] since both algorithms use the TV term and the sparsity term as regularizers. The main difference between the two algorithms lies in a) the use of the bilateral filter, i.e., the computation of $\mathbf{V}_3^{(k+1)}$, $\mathbf{V}_4^{(k+1)}$, $\mathbf{D}_3^{(k+1)}$, and $\mathbf{D}_4^{(k+1)}$ and b) the use of the reweighting matrix $\mathbf{W}^{(k)}$ when computing $\mathbf{V}_2^{(k+1)}$. We will evaluate the effectiveness of both the bilateral filter and the reweighting matrix in Section 4.

Algorithm 1 Pseudocode of the SUnSAL-BF-TV algorithm.

Initialization: Choose $\mathbf{V}_i^{(0)}$, $\mathbf{D}_i^{(0)}$, for $i = 1, \cdots, 6$, λ, λ_{bf}, μ, σ_s, and σ_r.

Repeat:

1) $\mathbf{X}^{(k+1)} = (\mathbf{A}^T\mathbf{A} + 3\mathbf{I})^{-1}\left(\mathbf{A}^T(\mathbf{V}_1^{(k)} + \mathbf{D}_1^{(k)}) + \mathbf{V}_2^{(k)} + \mathbf{D}_2^{(k)} + \mathbf{V}_3^{(k)} + \mathbf{D}_3^{(k)} + \mathbf{V}_6^{(k)} + \mathbf{D}_6^{(k)}\right)$

2) $\mathbf{V}_1^{(k+1)} = \frac{1}{1+\mu}\left(\mathbf{Y} + \mu(\mathbf{A}\mathbf{X}^{(k+1)} - \mathbf{D}_1^{(k)})\right)$

3) $\mathbf{W}_{i,j}^{(k)} = \frac{1}{\left|\left(\mathbf{X}^{(k+1)} - \mathbf{D}_2^{(k)}\right)_{i,j}\right| + \epsilon}$ for $\epsilon = 10^{-16}$

4) $\mathbf{V}_2^{(k+1)} = \text{soft}(\mathbf{X}^{(k+1)} - \mathbf{D}_2^{(k)}, \frac{\lambda}{\mu}\mathbf{W}^{(k)})$

5) $\mathbf{V}_3^{(k+1)} = \frac{1}{2}(\mathbf{V}_4^{(k)} + \mathbf{D}_4^{(k)}) + \frac{1}{2}(\mathbf{X}^{(k+1)} - \mathbf{D}_3^{(k)})$

6) $\mathbf{V}_4^{(k+1)} = (\mathbf{I} + \mathbf{H}^T\mathbf{H})^{-1}\left(\mathbf{B}\mathbf{F}(\mathbf{V}_3^{(k+1)}) - \mathbf{D}_4^{(k)} + \mathbf{H}^T(\mathbf{V}_5^{(k)} + \mathbf{D}_5^{(k)})\right)$

7) $\mathbf{V}_5^{(k+1)} = \text{soft}(\mathbf{H}\mathbf{V}_4^{(k+1)} - \mathbf{D}_5^{(k)}, \frac{\lambda_{bf}}{\mu})$

8) $\mathbf{V}_6^{(k+1)} = \max(\mathbf{X}^{(k+1)} - \mathbf{D}_6^{(k)}, \mathbf{0})$

Update Lagrange multipliers:

9) $\mathbf{D}_1^{(k+1)} = \mathbf{D}_1^{(k)} - \mathbf{A}\mathbf{X}^{(k+1)} + \mathbf{V}_1^{(k+1)}$

10) $\mathbf{D}_2^{(k+1)} = \mathbf{D}_2^{(k)} - \mathbf{X}^{(k+1)} + \mathbf{V}_2^{(k+1)}$

11) $\mathbf{D}_3^{(k+1)} = \mathbf{D}_3^{(k)} - \mathbf{X}^{(k+1)} + \mathbf{V}_3^{(k+1)}$

12) $\mathbf{D}_4^{(k+1)} = \mathbf{D}_4^{(k)} - \mathbf{B}\mathbf{F}(\mathbf{V}_3^{(k+1)}) + \mathbf{V}_4^{(k+1)}$

13) $\mathbf{D}_5^{(k+1)} = \mathbf{D}_5^{(k)} - \mathbf{H}\mathbf{V}_4^{(k+1)} + \mathbf{V}_5^{(k+1)}$

14) $\mathbf{D}_6^{(k+1)} = \mathbf{D}_6^{(k)} - \mathbf{X}^{(k+1)} + \mathbf{V}_6^{(k+1)}$

Until: some stopping criterion is satisfied.

4. Experiments with synthetic data

In this section, we indicate the effectiveness of the proposed unmixing algorithm SUnSAL-BF-TV on two simulated hyperspectral data sets. We will compare SUnSAL-BF-TV with four effective unmixing algorithms: SUnSAL [7], CLSUnSAL [15], ADSpLRU [24],[1] and SUnSAL-TV [21].[2]

For quantitative analysis, the signal-to-reconstruction error (SRE), measured in dB, is used to evaluate the unmixing accuracy. It is defined by

$$\text{SRE (dB)} = 10\log_{10}\frac{\mathbb{E}[\|\mathbf{X}\|_F^2]}{\mathbb{E}[\|\mathbf{X} - \hat{\mathbf{X}}\|_F^2]}, \tag{9}$$

where $\mathbb{E}$ denotes the expected value, $\hat{\mathbf{X}}$ and $\mathbf{X}$ are the estimated and true abundances, respectively. Generally speaking, the higher SRE values, the higher the quality of the unmixing results. To obtain the highest SREs, we select the optimal parameter λ for SUnSAL and CLSUnSAL from the following sequence: {0.0005, 0.001, 0.005, 0.01, 0.05, 0.5, 1, 5}. Similarly, after empirical optimization, we search the optimal λ and λ_{TV} for SUnSAL-TV, λ and λ_{bf} for SUnSAL-BF-TV, and the sparse parameter γ and the low-rank parameter τ for ADSpLRU, from the sequence

$$\{0.0005,\ 0.001,\ 0.005,\ 0.01,\ 0.05\ \ 0.5,\ 1,\ 5,\ 10\}. \tag{10}$$

All possible combinations of the parameters in (10) are considered. We note that each of SUnSAL and CLSUnSAL has only one regularization parameter, but each of SUnSAL-TV, ADSpLRU, and SUnSAL-BF-TV has two. Thus, choosing the best parameters of SUnSAL-TV, ADSpLRU, and SUnSAL-BF-TV costs much more computational time than that of SUnSAL and CLSUnSAL. In addition, we fix the spatial parameter $\sigma_s = 18$ and the range parameter $\sigma_r = 0.005$ for the bilateral filter in SUnSAL-BF-TV and set the Lagrange parameter $\mu = 0.1$ for all algorithms. For all the experiments, we stop the SUnSAL-BF-TV algorithm if

$$\left\|\mathbf{G}\mathbf{X}^{(k)} + \mathbf{B}\mathbf{V}^{(k)}\right\|_F \leq 5 \times 10^{-5}$$

or the maximum iteration number reached 500. All the tests are performed by using MATLAB R2016a on the platform of Windows 10 with 1.80 GHz Intel Core i5-3337U and 8GB memory. The floating-point precision is 10^{-16}.

4.1. Simulated data sets

For the simulated data sets, we use the spectral library $\mathbf{A} \in \mathbb{R}^{100\times120}$, which has been also used in [19,22,45,46]. It is a subset of a library of 262 spectral signatures with 100 spectral bands generally found on satellites, from the National Aeronautics and Space Administration (NASA) Johnson Space Center (JSC) Spacecraft Materials Spectral Database [47].

[1] The MATLAB code of ADSpLRU is available at http://members.noa.gr/parisg/demo_splr_unmixing.zip.

[2] The MATLAB codes of SUnSAL, CLSUnSAL, and SUnSAL-TV are available at http://www.lx.it.pt/~bioucas/publications.html.

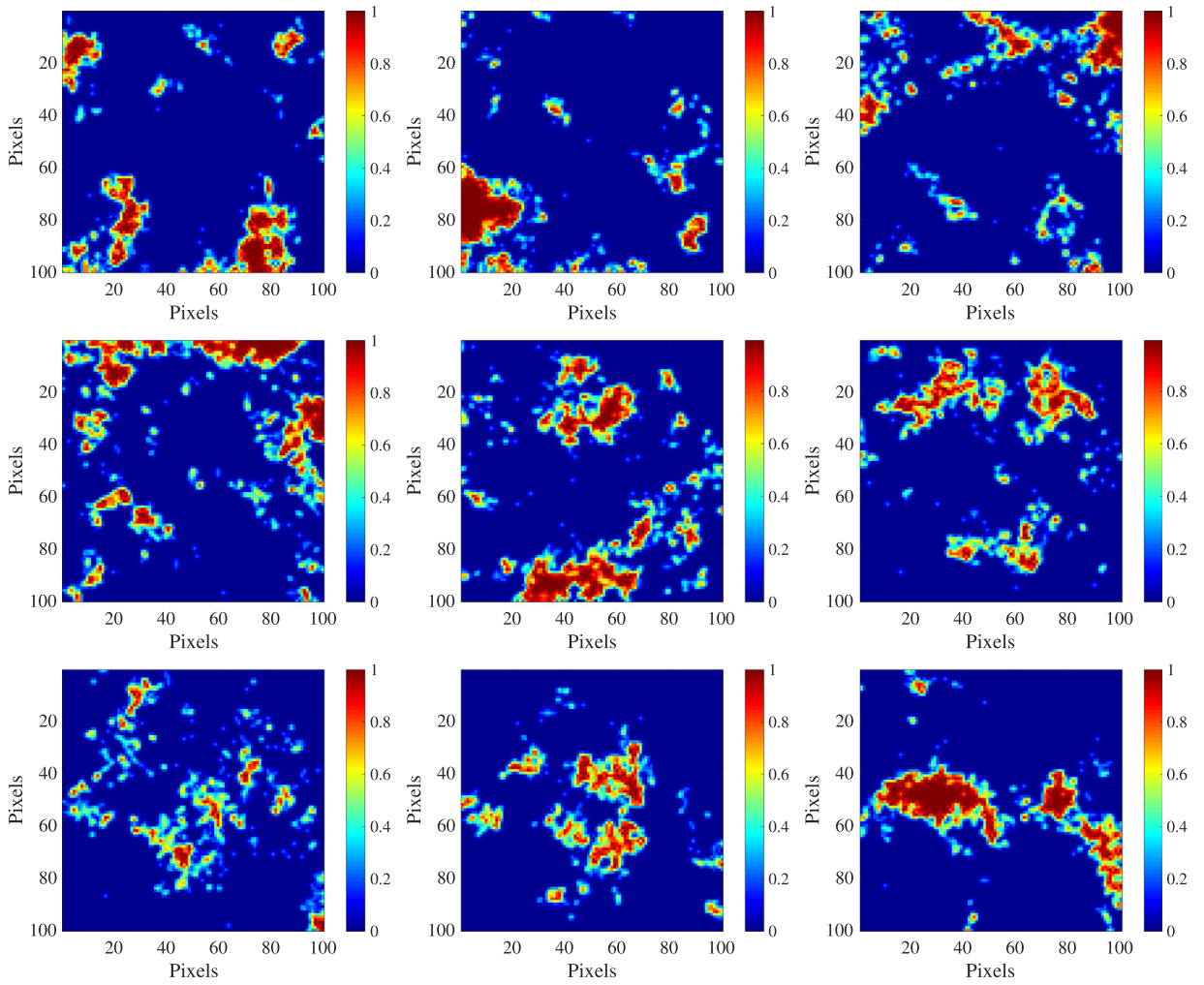

Fig. 3. True abundance maps of the endmembers in Data1. The first row: (from left to right) endmembers #1–#3. The second row: (from left to right) endmembers #4–#6. The last row: (from left to right) endmembers #7–#9.

1. *Simulated Data Cube 1* (Data1): The first simulated data cube contains 100×100 pixels with 100 bands per pixel. We generate the test data according to LMM by nine randomly selected signatures from **A**. Fig. 3 shows the true abundances[3] of the selected endmembers. After generating the data cube, we contaminate the simulated hyperspectral image by white Gaussian noise for three levels of the signal-to-noise ratio (SNR): 20, 30, and 40 dB.
2. *Simulated Data Cube 2* (Data2): In the second data cube, we choose a simulated hyperspectral image of the Hubble Space Telescope, similarly as in [22,45]. The data cube, of size $128 \times 128 \times 100$, is a simulation of that collected by the U.S Air Force AEOS Spectral Imaging Sensor (ASIS) [48]. Twelve signatures are randomly selected from **A** and then used to generate the data according to LMM. The corresponding true fractional abundances[4] are shown in Fig. 4. After the above procedure, the simulated hyperspectral data is contaminated by Gaussian noise with the same SNR values adopted for Data1.

4.2. Comparisons of different unmixing algorithms

We now show the effectiveness of SUnSAL-BF-TV in comparison with SUnSAL, CLSUnSAL, SUnSAL-TV, and ADSpLRU. Table 1 lists the SRE (dB) values and the elapsed CPU time in seconds [denoted by Time (s)] achieved by different unmixing algorithms for Data1 and Data2 with SNR = 20, 30, and 40 dB. Optimal regularization parameters for the compared algorithms are also provided in the parentheses. For further comparisons, Figs. 5 and 6 show the estimated abundance maps

[3] http://www.lx.it.pt/~bioucas/publications.html.
[4] http://www.escience.cn/people/miv/publication.html.

Table 1
SRE (dB) and Time (s) values achieved by different unmixing algorithms for Data1 and Data2.

Data1						
SNR		SUnSAL	CLSUnSAL	SUnSAL-TV	ADSpLRU	SUnSAL-BF-TV
20dB	SRE Time	2.05 76.67 ($\lambda = 0.05$)	1.23 121.72($\lambda = 1.00$)	5.98 350.01 ($\lambda = 0.01$, $\lambda_{TV} = 0.01$)	2.65 221.95 ($\gamma = 0.01$, $\tau = 5$)	**9.41** 422.87 ($\lambda = 0.01$, $\lambda_{bf} = 0.01$**)**
30dB	SRE Time	8.12 58.97 ($\lambda = 0.05$)	7.23 65.23 ($\lambda = 1.00$)	12.87 351.92 ($\lambda = 0.01$, $\lambda_{TV} = 0.005$)	16.09 243.11 ($\gamma = 0.01$, $\tau = 1$)	**16.90** 425.77 ($\lambda = 0.001$, $\lambda_{bf} = 0.005$**)**
40dB	SRE Time	11.04 57.99 ($\lambda = 0.01$)	17.05 73.54 ($\lambda = 0.10$)	20.23 264.21 ($\lambda = 0.005$, $\lambda_{TV} = 0.001$)	**26.23** 233.21 ($\gamma = 0.0005$, $\tau = 0.5$**)**	23.08 413.03 ($\lambda = 0.0005$, $\lambda_{bf} = 0.001$)
				Data2		
SNR		SUnSAL	CLSUnSAL	SUnSAL-TV	ADSpLRU	SUnSAL-BF-TV
20dB	SRE Time	3.32 121.72 ($\lambda = 0.01$)	3.17 123.37 ($\lambda = 0.05$)	7.41 391.01 ($\lambda = 0.01$, $\lambda_{TV} = 0.005$)	5.54 525.94 ($\gamma = 0.001$, $\tau = 5$)	**10.15** 374.98 ($\lambda = 0.005$, $\lambda_{bf} = 0.005$**)**
30dB	SRE Time	11.55 123.75($\lambda = 0.005$)	11.95 126.94 ($\lambda = 0.05$)	16.98 440.19 ($\lambda = 0.01$, $\lambda_{TV} = 0.001$)	22.89 474.64 ($\gamma = 0.005$, $\tau = 0.5$)	**27.21** 376.57 ($\lambda = 0.001$, $\lambda_{bf} = 0.001$**)**
40dB	SRE Time	21.98 122.35 ($\lambda = 0.005$)	24.47 121.32($\lambda = 0.05$)	25.07420.91 ($\lambda = 0.005$, $\lambda_{TV} = 0.0005$)	36.01 511.48 ($\gamma = 0.001$, $\tau = 0.1$)	**40.38** 426.29 ($\lambda = 0.001$, $\lambda_{bf} = 0.001$**)**

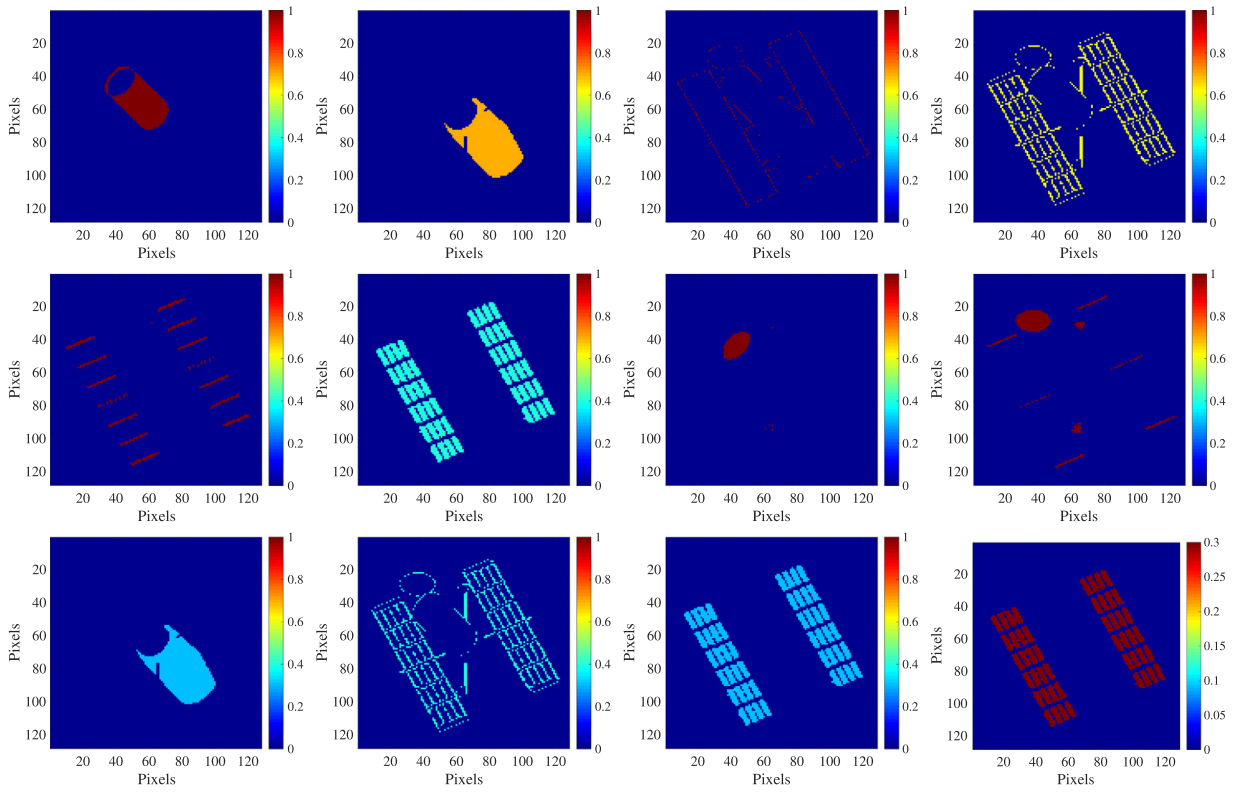

Fig. 4. True abundance maps of the endmembers in Data2. The first row: (from left to right) Endmembers #1–#4. The second row: (from left to right) Endmembers #5–#8. The last row: (from left to right) Endmembers #9–#12.

for endmembers #5 and #9 in Data1, respectively. Similarly for Data2, Figs. 7 and 8 show the estimated abundance maps for endmembers #4 and #12, respectively. Other estimated abundance maps show similar behavior, so we omit here for space considerations.

Clearly, we see from Table 1 that SUnSAL-BF-TV provides higher SRE values than SUnSAL, CLSUnSAL, SUnSAL-TV, and ADSpLRU for both data cubes except for one case (Data1 with SNR = 40 dB). For higher noise levels like SNR = 20 and 30 dB, both SUnSAL and CLSUnSAL, each of which has only one regularization term, provide much lower SRE values. For SNR = 20 dB, ADSpLRU provides the lowest SRE values among the three unmixing algorithms having two regularization terms. For SNR = 30 and 40 dB, however, ADSpLRU provides better results than SUnSAL-TV. Clearly, the proposed SUnSAL-BF-TV algorithm provides higher or comparable SREs for both data cubes with all SNR levels. In particular, the improvement of SUnSAL-BF-TV, in comparison to SUnSAL-TV, on SRE is more than 10 dB for Data2 with SNR of 30 and 40 dB. Also, for the higher noise level of 20 dB, the improvement on SRE is greater than 2 dB for both data cubes. Besides, we see from Table 1 that SUnSAL and CLSUnSAL are very fast. In comparison with SUnSAL-TV, SUnSAL-BF-TV costs more or comparable computational time. It can be expected since we have used the bilateral filter at each iteration.

From Figs. 5 and 6, we see that for the lower noise level of SNR = 40 dB, all compared unmixing algorithms attain similar abundance maps with the accurate spatial distribution. For SNR with 20 and 30 dB, however, SUnSAL-BF-TV gives smoother background and better delineates high fractional abundance regions than the other four unmixing algorithms. In particular, the abundance maps obtained by SUnSAL-TV for SNR = 20 and 30 dB show a clear staircase effect, whereas SUnSAL-BF-TV, as expected, addresses the staircase effect and provides satisfactory estimations. Similar conclusions can be obtained for Data2 from Figs. 7 and 8. In conclusion, for both data cubes, SUnSAL-BF-TV estimates the abundance maps with better accuracy, which is significantly clear for higher noise levels of SNR = 20 and 30 dB. These observations are in line with those already recorded in Table 1.

Furthermore, we show the ground-truth and estimated abundances of selected 100 adjacent pixels of Data1 with SNR = 30 dB in Fig. 9. We see from Fig. 9 that there are many low abundance values estimated by SUnSAL, CLSUnSAL, and SUnSAL-TV that are not actually present in the abundance. ADSpLRU and SUnSAL-BF-TV provide more accurate estimated abundances. However, the background by ADSpLRU is slightly less smooth than that by SUnSAL-BF-TV. Therefore, we conclude that the lines (denoting the abundance of a certain endmember in all pixels of the image) estimated by SUnSAL-BF-TV are more similar to those in the ground-truth than the ones estimated by SUnSAL, CLSUnSAL, SUnSAL-TV, and ADSpLRU.

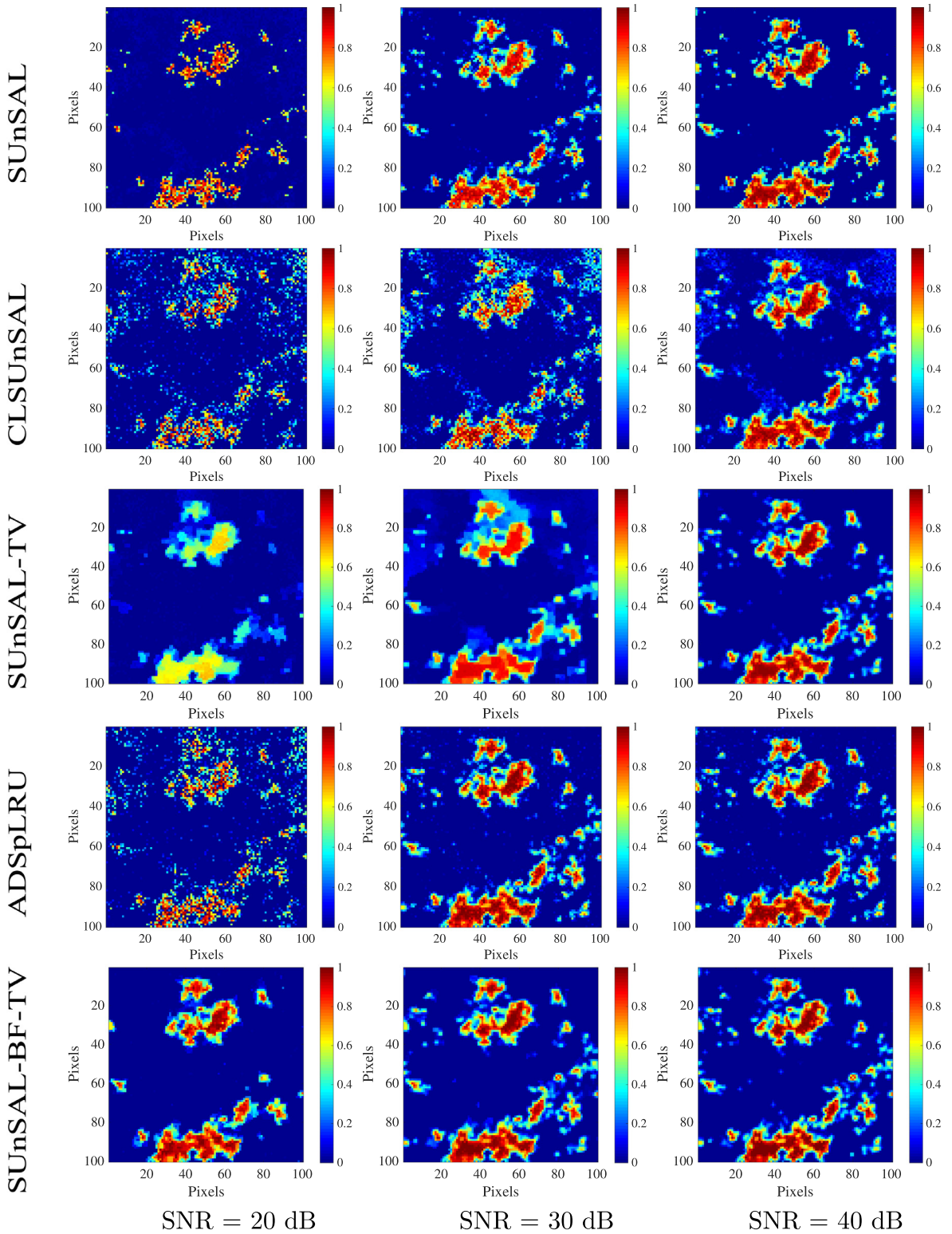

Fig. 5. Estimated abundance maps by different unmixing algorithms for endmember #5 in Data1 with different SNRs.

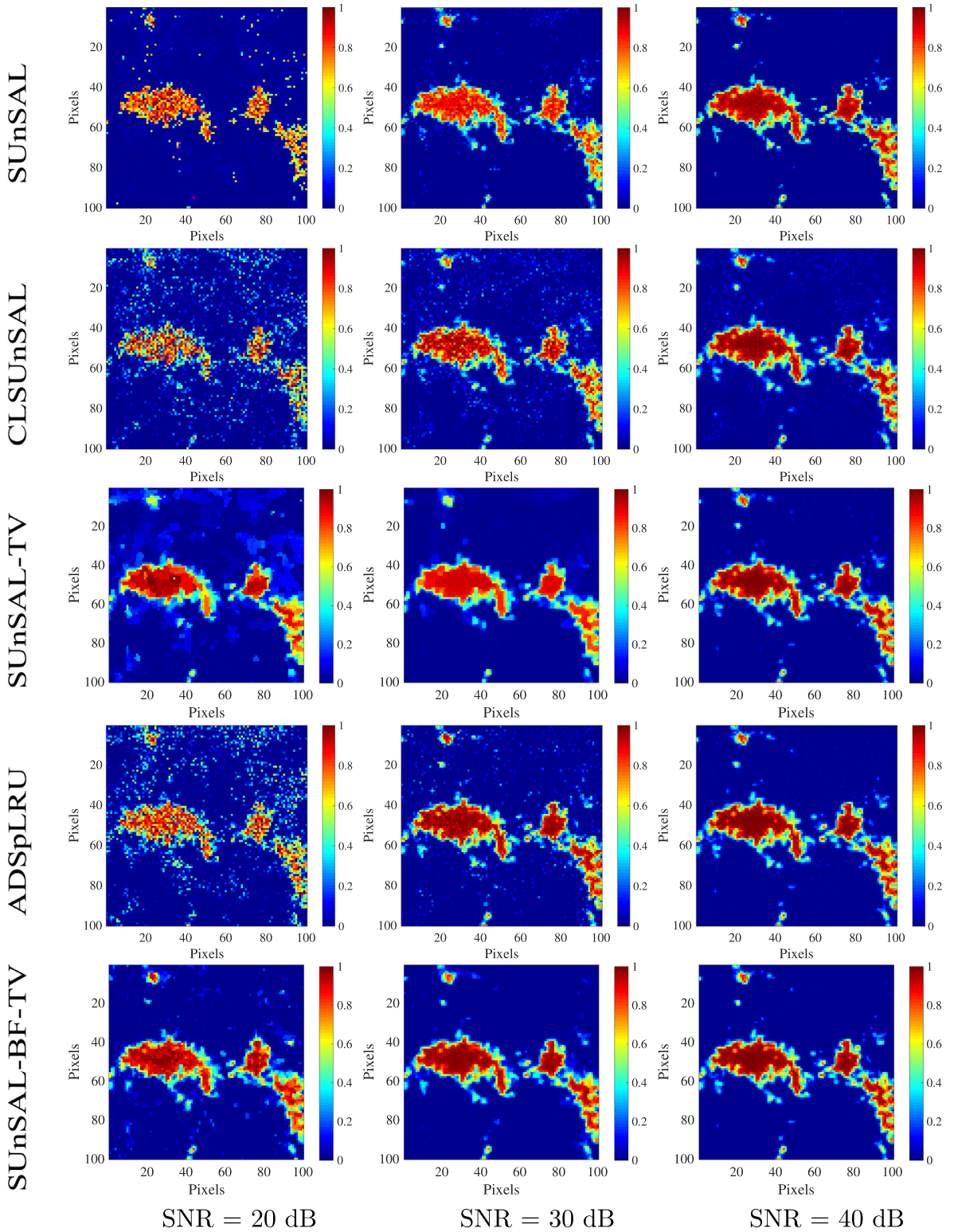

Fig. 6. Estimated abundance maps by different unmixing algorithms for endmember #9 in Data1 with different SNRs.

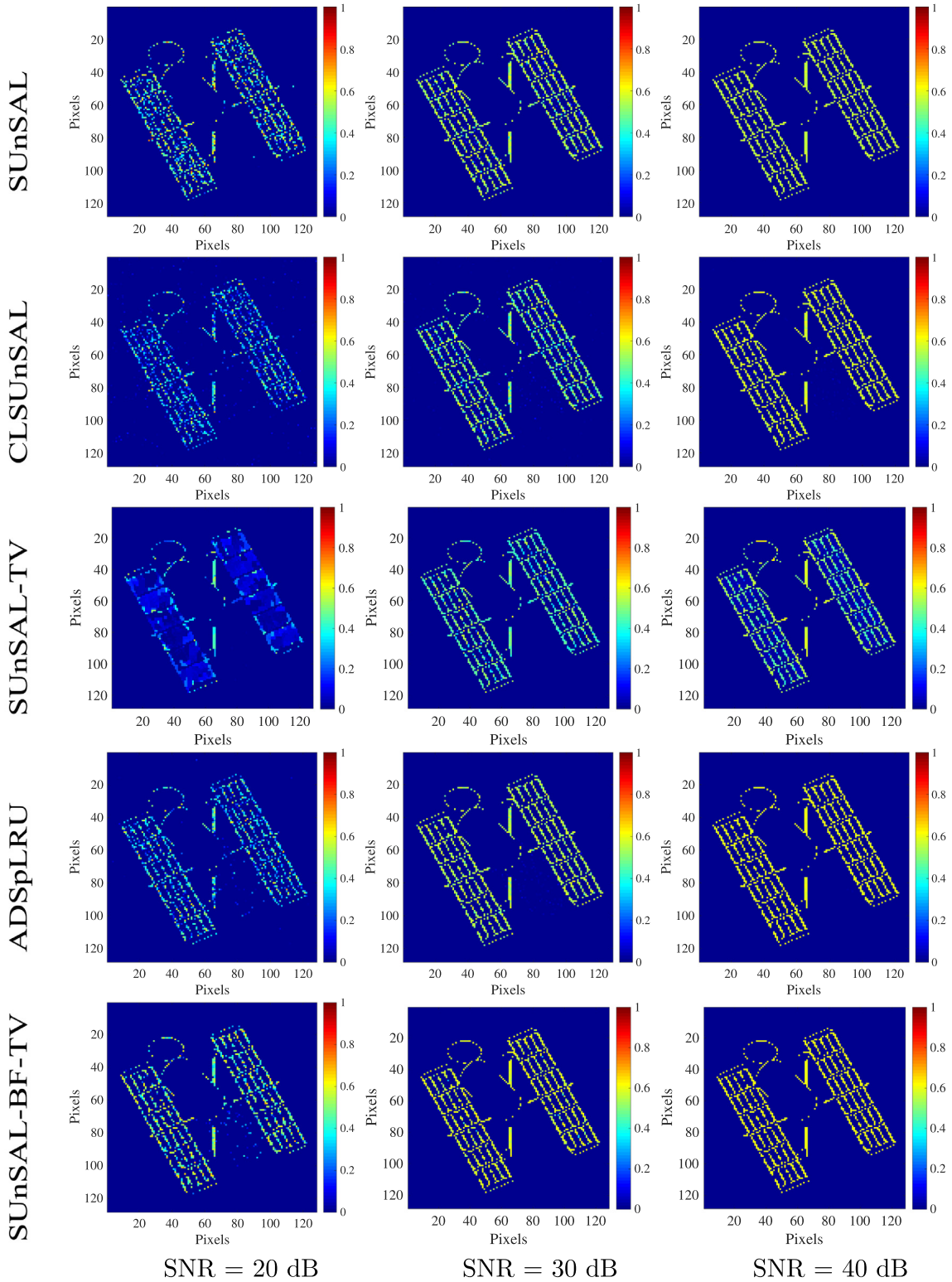

Fig. 7. Estimated abundance maps by different unmixing algorithms for endmember #4 in Data2 with different SNRs.

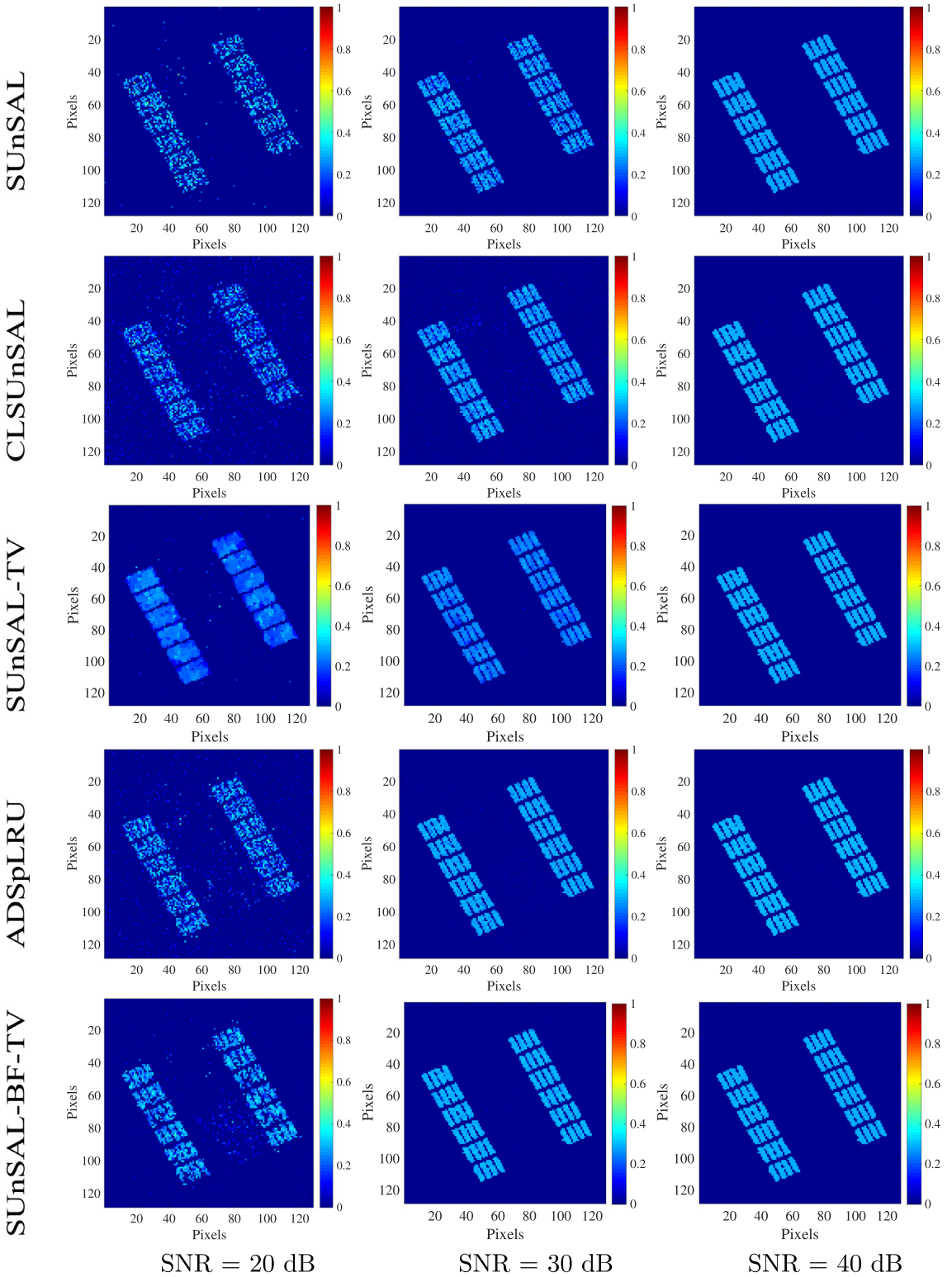

Fig. 8. Estimated abundance maps by different unmixing algorithms for endmember #12 in Data2 with different SNRs.

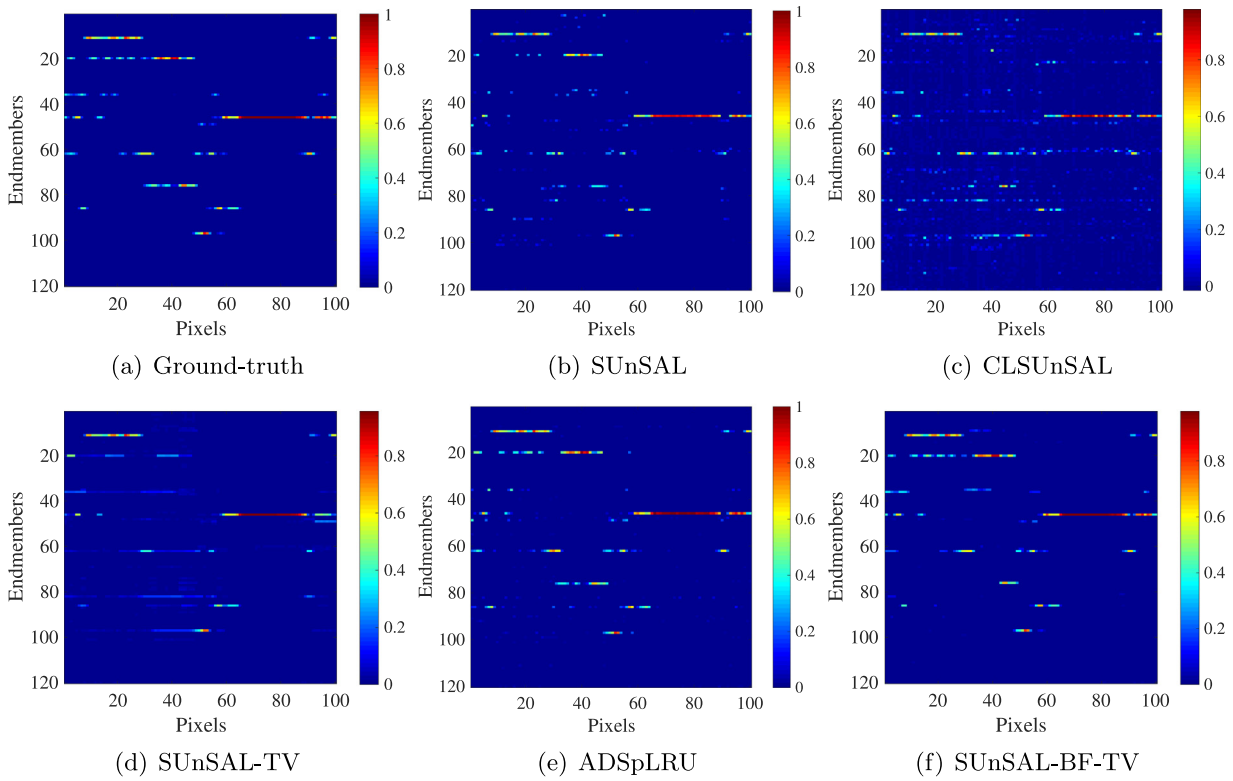

Fig. 9. Ground-truth and estimated abundances for 100 selected adjacent pixels for Data1 with SNR = 30 dB by different unmixing algorithms.

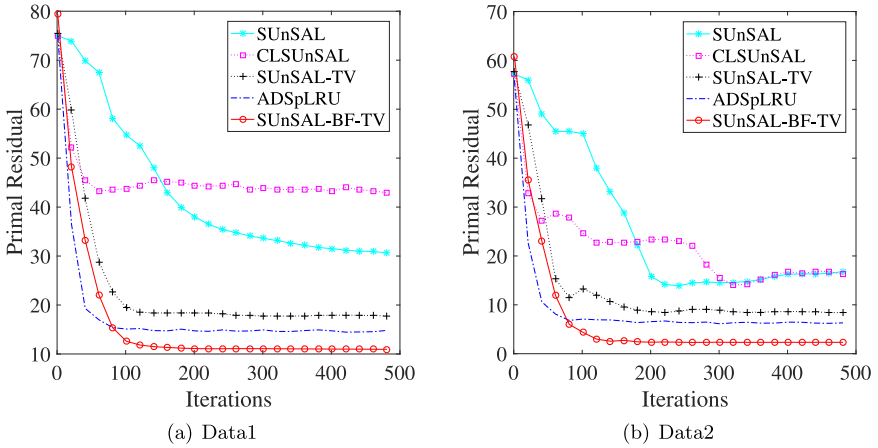

Fig. 10. Primal residual $\|\mathbf{GX}^{(k)} + \mathbf{BV}^{(k)}\|_F$ versus the iteration number k with SNR = 30 dB for different unmixing algorithms.

Finally, Fig. 10 plots the primal residual, i.e., $\|\mathbf{GX}^{(k)} + \mathbf{BV}^{(k)}\|_F$, versus the iteration number k by different unmixing algorithms for both Data1 and Data2 with SNR = 30 dB. We see that SUnSAL-BF-TV attains the lowest primal residuals than the other four compared unmixing algorithms. In addition, though there is no theoretical guarantee, SUnSAL-BF-TV, ADSpLRU, and SUnSAL-TV numerically exhibit a robust convergence behavior for both data cubes.

4.3. Parameter selections of SUnSAL-BF-TV

In this subsection, we first show the role of parameters λ and λ_{bf} in SUnSAL-BF-TV and then study the robustness of parameters μ, σ_s, and σ_r, similarly as in [49]. Finally, we investigate the effectiveness of the reweighting matrix $\mathbf{W}^{(k)}$ in (8) by comparing SUnSAL-BF-TV with/without adopting the reweighting matrix $\mathbf{W}^{(k)}$ with SUnSAL-TV.

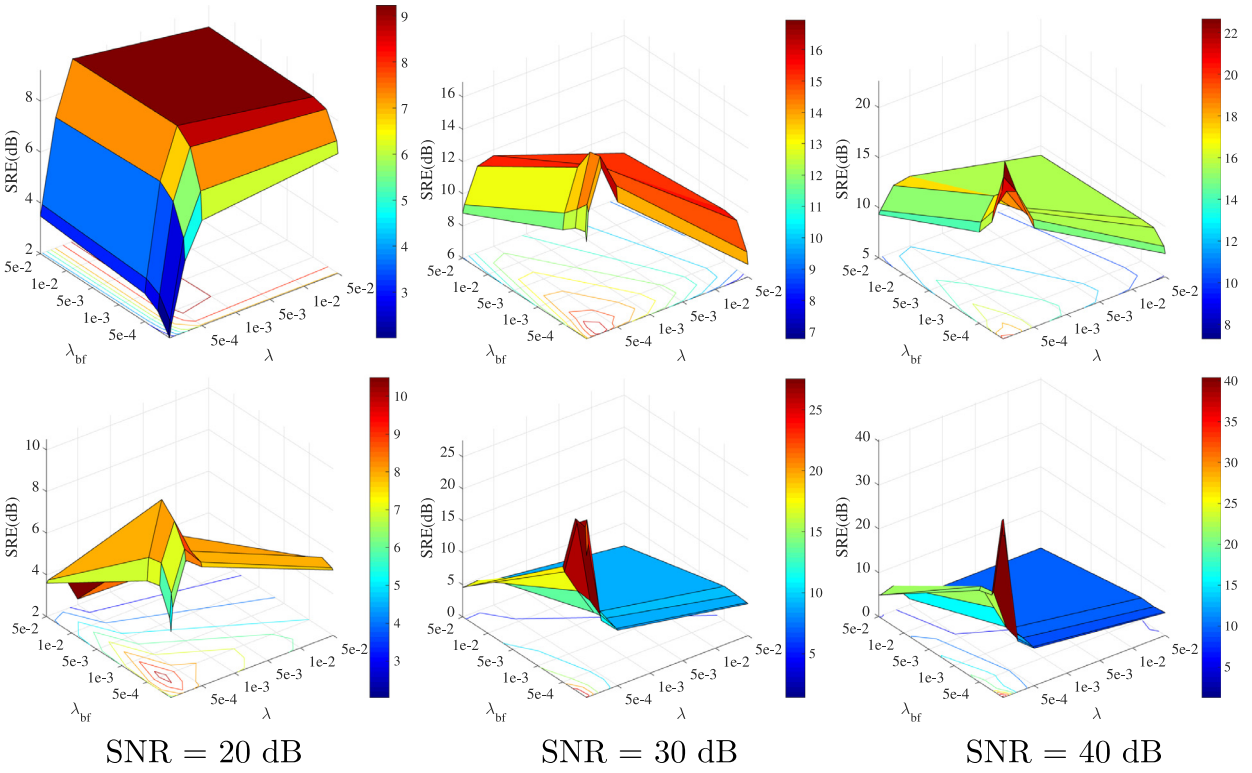

Fig. 11. SRE (dB) as a function of parameters λ and λ_{bf} for (top row) Data1 and (bottom row) Data2 with different SNR levels.

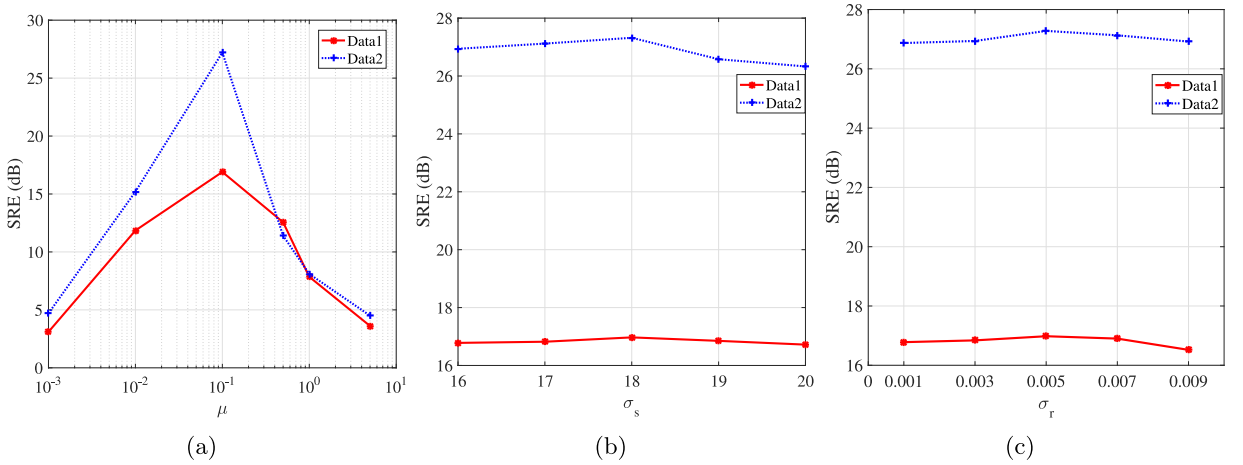

Fig. 12. SRE (dB) as a function of parameters (a) μ, (b) σ_s, and (c) σ_r for Data1 and Data2 with SNR = 30 dB.

From the model in (3), we see that the regularization parameters λ and λ_{bf} control the tradeoff between sparsity in the abundance and sparsity in the gradient domain. In our experiments, we consider all possible combinations of λ and λ_{bf} in the sequence (10) and select the optimal parameter values with respect to highest SRE values. Fig. 11 shows the obtained SRE (dB) values as a function of λ and λ_{bf} for Data1 and Data2 with different noise levels. From Fig. 11, we can see that the optimal parameters of SUnSAL-BF-TV increase as the noise level becomes higher for both data sets. In addition, each of λ and λ_{bf} plays an important role in abundance estimation. It shows the effectiveness of both the sparsity term and the bilateral filter based TV term in (3). Generally, for SUnSAL-BF-TV, optimal λ_{bf} is higher than or equal to optimal λ, which is consistent with the quantitative observation from Table 1.

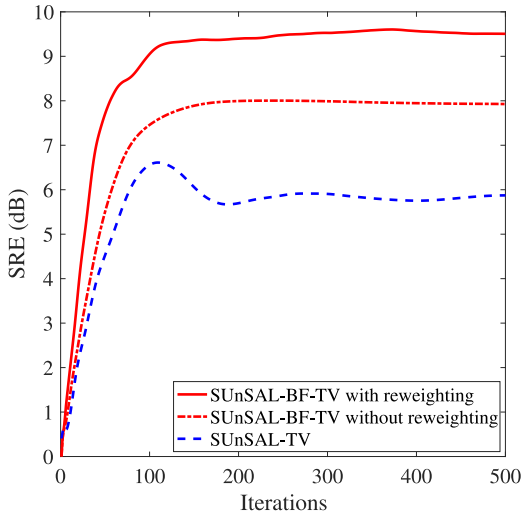

Fig. 13. SRE (dB) results provided by different unmixing algorithms for Data1 with SNR = 20 dB.

Fig. 12 shows the SRE(dB) values as a function of μ, σ_s, and σ_r for Data1 and Data2 with SNR = 30 dB. From this figure, we can see that σ_s and σ_r are robust for each data set. However, we have to carefully choose the value of μ to obtain better results, similarly as in SUnSAL-TV and ADSpLRU. With these observations, we fix $\mu = 0.1$, $\sigma_s = 18$, and $\sigma_r = 0.005$ in our experiments for both simulated and real data sets.

Finally, we show the effectiveness of the reweighting matrix $\mathbf{W}^{(k)}$ in (8). For this purpose, Fig. 13 plots the SRE values against the iteration number for SUnSAL-BF-TV with and without the reweighting matrix for Data1 with SNR = 20 dB. The curves of SUnSAL-TV are also provided for comparison. We can see from Fig. 13 that both SUnSAL-BF-TV with and without the reweighting matrix $\mathbf{W}^{(k)}$ provide higher SRE values than SUnSAL-TV as iteration becomes stable. In addition, the SUnSAL-BF-TV algorithm with the reweighting matrix $\mathbf{W}^{(k)}$ is clearly better than the algorithm without one. It thus shows the effectiveness of the reweighting strategy, and also the effectiveness of the bilateral filter, in the proposed SUnSAL-BF-TV algorithm.

5. Experiment with real data

In this experiment, we illustrate the performance of SUnSAL-BF-TV on the well-known Airborne Visible/Infrared Imaging Spectrometer (AVIRIS) hyperspectral image of Cuprite.[5] We use a portion of 200×200 pixels with 188 spectral bands, which corresponds to a subset of the sector labeled as $f970619t01p02\_r02\_\{s\}c03.a.rfl$ in the online data; see [7,21] for more details. The 188×240 spectral library matrix in this experiment is generated from the U.S. Geological Survey (USGS) spectral library (splib06a),[6] which includes all exposed minerals of interest. Fig. 14 shows a mineral map produced in 1995 by USGS, in which different minerals were mapped by a Tetracorder software product[7] [50]. Note that the detailed ground truth information is unavailable, we just qualitatively compare the performance of different unmixing algorithms with the minerals map by the Tetracorder 4.4 software product.

Fig. 15 shows the estimated fractional abundances of three different materials: *alunite, chalcedony*, and *muscovite*, by the Tetracorder 4.4 software product, SUnSAL, CLSUnSAL, SUnSAL-TV, ADSpLRU, and SUnSAL-BF-TV. Similarly as in [21], the regularization parameters, including λ for SUnSAL and CLSUnSAL and both λ and λ_{TV} for SUnSAL-TV, are set to 0.001. We also set the regularization parameters $\gamma = \tau = 0.001$ for ADSpLRU and the regularization parameters $\lambda = \lambda_{bf} = 0.001$ for SUnSAL-BF-TV. And similarly as in simulated experiments, we set $\sigma_s = 18$ and $\sigma_r = 0.005$ for the bilateral filter. From Fig. 15, we see that all five sparse unmixing algorithms produce similar abundance maps. We also see that SUnSAL-BF-TV gives generally higher or comparable abundances in the regions classified as respective minerals in comparison with SUnSAL, CLSUnSAL, SUnSAL-TV, and ADSpLRU. It shows that the SUnSAL-BF-TV algorithm is effective to unmix real hyperspectral data.

[5] Available online: http://aviris.jpl.nasa.gov/html/aviris.freedata.html.
[6] Available online: http://speclab.cr.usgs.gov/spectral.lib06.
[7] Available online: https://speclab.cr.usgs.gov/PAPERS/tetracorder/.

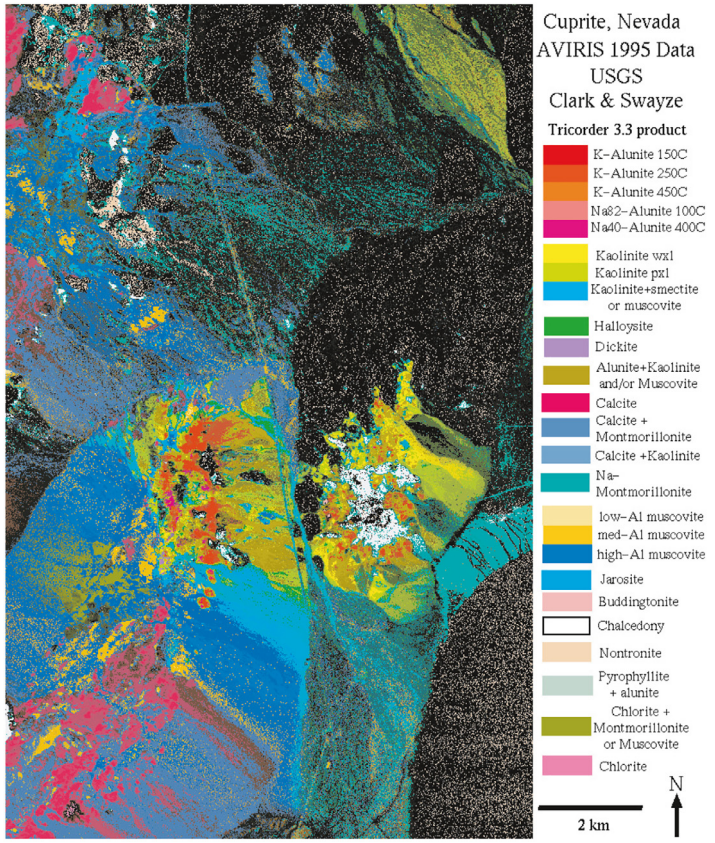

Fig. 14. USGS map showing the location of different minerals in the Cuprite mining district in Nevada. The map is available online at http://speclab.cr.usgs.gov/cuprite95.tgif.2.2um_map.gif.

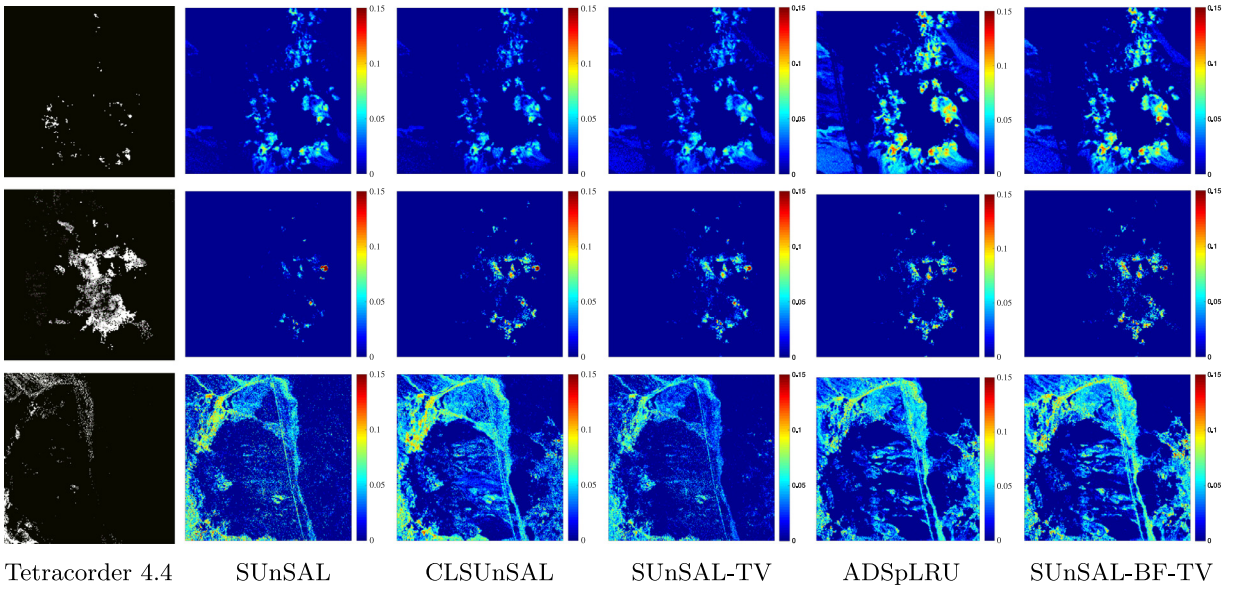

Fig. 15. Abundance maps estimated for three minerals: (from top row to bottom row) *alunite*, *chalcedony*, and *muscovite*, by Tetracorder 4.4 and different unmixing algorithms for the AVIRIS Cuprite scene.

6. Conclusion

In this paper, we have proposed a bilateral filter based TV spatial regularizer for sparse hyperspectral image unmixing. The main idea is to enforce the TV term on the bilateral filtered abundance maps, rather than directly on the abundance maps, to address the staircase effect of TV. In this vein, we promote the sparsity in the gradient domain as the bilateral filter smoothes images while maintaining edges. Then we have presented a model that combines both the bilateral filter based TV and sparsity regularization terms with the data-fidelity term. To solve the proposed model, we have designed an algorithm called SUnSAL-BF-TV under the ADMM framework. Simulated experiments have shown that the SUnSAL-BF-TV algorithm provides higher or comparable SRE values and more accurate abundance estimations than several popular unmixing algorithms. In addition, the proposed algorithm has shown to be effective to unmix real hyperspectral data. Finally, applying a 3-D bilateral filter for hyperspectral unmixing is currently under investigation.

Conflict of interest

We wish to confirm that there are no known conflicts of interest associated with this publication and there has been no significant financial support for this work that could have influenced its outcome.

Acknowledgments

The authors would like to express their thanks to the reviewers and Prof. Witold Pedrycz for their constructive, detailed, and helpful advice regarding this paper.

References

[1] J.B. Adams, M.O. Smith, P.E. Johnson, Spectral mixture modeling: a new analysis of rock and soil types at the Viking Lander 1 site, J. Geophys. Res. Atmos. 91 (1986) 8098–8112.
[2] A. Plaza, P. Martinez, R. Perez, J. Plaza, A quantitative and comparative analysis of endmember extraction algorithms from hyperspectral data, IEEE Trans. Geosci. Remote Sens. 42 (3) (2004) 650–663.
[3] Q. Du, N. Raksuntorn, N. Younan, R. King, Endmember extraction for hyperspectral image analysis., Appl. Opt. 47 (28) (2008) 77–84.
[4] G.X. Ritter, G. Urcid, A lattice matrix method for hyperspectral image unmixing, Inf. Sci. 181 (10) (2011) 1787–1803.
[5] C.-I. Chang, Hyperspectral Imaging: Techniques for Spectral Detection and Classification, Plenum Publishing Co., 2003.
[6] J.M. Bioucas-Dias, M.A.T. Figueiredo, Alternating direction algorithms for constrained sparse regression: application to hyperspectral unmixing, in: The Workshop on Hyperspectral Image Signal Processing: Evolution in Remote Sensing, 2010, pp. 1–4.
[7] M.D. Iordache, J.M. Bioucas-Dias, A. Plaza, Sparse unmixing of hyperspectral data, IEEE Trans. Geosci. Remote Sens. 49 (6) (2011) 2014–2039.
[8] L. Sun, Z. Wu, L. Xiao, J. Liu, Z. Wei, F. Dang, A novel $l_{1/2}$ sparse regression method for hyperspectral unmixing, Int. J. Remote Sens. 34 (20) (2013) 6983–7001.
[9] Y.Z. Cheng, L. Hong, W. Qiong, C.L.P. Chen, Reweighted sparse regression for hyperspectral unmixing, IEEE Trans. Geosci. Remote Sens. 54 (1) (2015) 479–488.
[10] W. Tang, Z.W. Shi, Y. Wu, C.S. Zhang, Sparse unmixing of hyperspectral data using spectral a priori information, IEEE Trans. Geosci. Remote Sens. 53 (2) (2016) 770–783.
[11] D. Hong, N. Yokoya, J. Chanussot, X.X. Zhu, An augmented linear mixing model to address spectral variability for hyperspectral unmixing, IEEE Trans. Image Process. 28 (2019) 1923–1938.
[12] J. Yu, Y. Rui, D. Tao, Click prediction for web image reranking using multimodal sparse coding, IEEE Trans. Image Process. 23 (5) (2014) 2019–2032.
[13] J. Huang, T.-Z. Huang, A nonstationary accelerating alternating direction method for frame-based Poissonian image deblurring, J. Comput. Applied Math. 352 (2019) 181–193.
[14] L. Sun, W. Ge, Y. Chen, J. Zhang, B. Jeon, Hyperspectral unmixing employing $l_1 - l_2$ sparsity and total variation regularization, Int. J. Remote Sens. 39 (19) (2018) 6037–6060.
[15] M.D. Iordache, J.M. Bioucas-Dias, A. Plaza, Collaborative sparse regression for hyperspectral unmixing, IEEE Trans. Geosci. Remote Sens. 52 (1) (2014) 341–354.
[16] J. Yao, D. Meng, Q. Zhao, W. Cao, Z. Xu, Nonconvex-sparsity and nonlocal-smoothness-based blind hyperspectral unmixing, IEEE Trans. Image Process. 28 (6) (2019) 2991–3006.
[17] S. Zhang, J. Li, H.-C. Li, C. Deng, A. Plaza, Spectral-spatial weighted sparse regression for hyperspectral image unmixing, IEEE Trans. Geosci. Remote Sens. 56 (6) (2018) 3265–3276.
[18] S. Zhang, J. Li, Z. Wu, A. Plaza, Spatial discontinuity-weighted sparse unmixing of hyperspectral images, IEEE Trans. Geosci. Remote Sens. 56 (10) (2018) 5767–5779.
[19] J. Huang, T.-Z. Huang, L.-J. Deng, X.-L. Zhao, Joint-sparse-blocks and low-rank representation for hyperspectral unmixing, IEEE Trans. Geosci. Remote Sens. 57 (4) (2019) 2419–2438.
[20] G. Martin, A. Plaza, Region-based spatial preprocessing for endmember extraction and spectral unmixing, IEEE Geosci. Remote Sens. Lett. 8 (4) (2011) 745–749.
[21] M.D. Iordache, J.M. Bioucas-Dias, A. Plaza, Total variation spatial regularization for sparse hyperspectral unmixing, IEEE Trans. Geosci. Remote Sens. 50 (11) (2012) 4484–4502.
[22] X.-L. Zhao, F. Wang, T.-Z. Huang, M. Ng, R. Plemmons, Deblurring and sparse unmixing for hyperspectral images, IEEE Trans. Geosci. Remote Sens. 51 (7) (2013) 4045–4058.
[23] Q. Qu, N.M. Nasrabadi, T.D. Tran, Abundance estimation for bilinear mixture models via joint sparse and low-rank representation, IEEE Trans. Geosci. Remote Sens. 52 (7) (2014) 4404–4423.
[24] P. Giampouras, K. Themelis, A. Rontogiannis, K. Koutroumbas, Simultaneously sparse and low-rank abundance matrix estimation for hyperspectral image unmixing, IEEE Trans. Geosci. Remote Sens. 54 (8) (2016) 4775–4789.
[25] H.K. Aggarwal, A. Majumdar, Hyperspectral unmixing in the presence of mixed noise using joint-sparsity and total variation, IEEE J. Sel. Topics Appl. Earth Observ. Remote Sens. 9 (9) (2016) 4257–4266.
[26] J. Sigurdsson, M.O. Ulfarsson, J.R. Sveinsson, Blind hyperspectral unmixing using total variation and ℓ_q sparse regularization, IEEE Trans. Geosci. Remote Sens. 54 (11) (2016) 6371–6384.
[27] W. He, H. Zhang, L. Zhang, Total variation regularized reweighted sparse nonnegative matrix factorization for hyperspectral unmixing, IEEE Trans. Geosci. Remote Sens. 55 (7) (2017) 3909–3921.

[28] F. Xiong, Y. Qian, J. Zhou, Y.Y. Tang, Hyperspectral unmixing via total variation regularized nonnegative tensor factorization, IEEE Trans. Geosci. Remote Sens. 57 (4) (2019) 2341–2357.
[29] X. Feng, H. Li, J. Li, Q. Du, A. Plaza, W.J. Emery, Hyperspectral unmixing using sparsity-constrained deep nonnegative matrix factorization with total variation, IEEE Trans. Geosci. Remote Sens. 56 (10) (2018) 6245–6257.
[30] X. Wang, Y. Zhong, L. Zhang, Y. Xu, Spatial group sparsity regularized nonnegative matrix factorization for hyperspectral unmixing, IEEE Trans. Geosci. Remote Sens. 55 (11) (2017) 6287–6304.
[31] M. Rizkinia, M. Okuda, Joint local abundance sparse unmixing for hyperspectral images, Remote Sens. 9 (12) (2017) 1224.
[32] T.-Y. Ji, T.-Z. Huang, X.-L. Zhao, T.-H. Ma, G. Liu, Tensor completion using total variation and low-rank matrix factorization, Inf. Sci. 326 (2016) 243–257.
[33] F. Fan, Y. Ma, C. Li, X. Mei, J. Huang, J. Ma, Hyperspectral image denoising with superpixel segmentation and low-rank representation, Inf. Sci. 397–398 (2017) 48–68.
[34] G.-Q. Ma, T.-Z. Huang, J. Huang, C.-C. Zheng, Local low-rank and sparse representation for hyperspectral image denoising, IEEE Access 7 (1) (2019) 79850–79865.
[35] J.-H. Yang, X.-L. Zhao, T.-H. Ma, Y. Chen, T.-Z. Huang, M. Ding, Remote sensing image destriping using unidirectional high-order total variation and nonconvex low-rank regularization, J. Comput. Applied Math. 363 (2020) 124–144.
[36] Y. Zhong, R. Feng, L. Zhang, Non-local sparse unmixing for hyperspectral remote sensing imagery, IEEE J. Sel. Topics Appl. Earth Observ. Remote Sens. 7 (6) (2014) 1889–1909.
[37] R. Wang, H.-C. Li, W. Liao, X. Huang, W. Philips, Centralized collaborative sparse unmixing for hyperspectral images, IEEE J. Sel. Topics Appl. Earth Observ. Remote Sens. 10 (3) (2017) 1949–1962.
[38] Y. Ma, C. Li, X.G. Mei, C.Y. Liu, J.Y. Ma, Robust sparse hyperspectral unmixing with $\ell_{2,1}$ norm, IEEE Trans. Geosci. Remote Sens. 55 (3) (2017) 1227–1239.
[39] J.-H. Yang, X.-L. Zhao, J.-J. Mei, S. Wang, T.-H. Ma, T.-Z. Huang, Total variation and high-order total variation adaptive model for restoring blurred images with Cauchy noise, Comput. Math. Appl. 77 (5) (2018) 1255–1272.
[40] L.-J. Deng, M. Feng, X.-C. Tai, The fusion of panchromatic and multispectral remote sensing images via tensor-based sparse modeling and hyper-Laplacian prior, Inf. Fusion 52 (2019) 76–89.
[41] C. Tomasi, R. Manduchi, Bilateral filtering for gray and color images, ICCV (1998) 839–846.
[42] S. Paris, P. Kornprobst, J. Tumblin, F. Durand, Bilateral filtering: theory and applications, Found. Trends Comput. Graph. Vis. 4 (1) (2008) 1–73.
[43] J. Yang, Y.-Q. Zhao, J. Chan, S. Kong, Coupled sparse denoising and unmixing with low-rank constraint for hyperspectral image, IEEE Trans. Geosci. Remote Sens. 54 (3) (2016) 1818–1833.
[44] E.J. Candès, M.B. Wakin, S.P. Boyd, Enhancing sparsity by reweighted ℓ_1 minimization, J. Fourier Anal. Appl. 14 (5) (2007) 877–905.
[45] F. Li, M. Ng, R. Plemmons, Coupled segmentation and denoising/deblurring models for hyperspectral material identification, Numer. Linear Algebra Appl. 19 (1) (2012) 153–173.
[46] G. Zhang, Y. Xu, F. Fang, Framelet-based sparse unmixing of hyperspectral images, IEEE Trans. Image Process. 25 (4) (2016) 1516–1529.
[47] K. Abercromby, Communication of the NASA JSC Spacecraft Materials Spectral Database, 2006.
[48] T. Blake, S. Cain, M. Goda, K. Jerkatis, Reconstruction of spectral images from the AEOS Spectral Imaging Sensor, in: Proc. AMOS Tech. Conf., 2006, pp. E1–E22.
[49] M. Mao, J. Lu, J. Han, G. Zhang, Multiobjective e-commerce recommendations based on hypergraph ranking, Inf. Sci. 471 (2019) 269–287.
[50] R. Clark et al., Imaging spectroscopy: Earth and planetary remote sensing with the USGS Tetracorder and expert systems, J. Geophys. Res. 108 (E12) (2003) 5131–5135.